Development and Performance Evaluation of Small SAR System for 100-kg Class Satellite

Budhaditya Pyne, *Member, IEEE*, Hirobumi Saito, *Member, IEEE*, Prilando Riziki Akbar, *Member, IEEE*, Jiro Hirokawa, *Fellow, IEEE*, Takashi Tomura, *Member, IEEE*, and Koji Tanaka, *Member, IEEE*

***Abstract*—This article shows development and performance evaluation of a MicroX-SAR demonstration satellite, scheduled to be launched in 2020 for synthetic aperture radar (SAR) application. This compact SAR system and its instruments are briefly described. The SAR antenna consists of deployable seven panels with a slot array and the antenna size is 4.9 × 0.7 m. This article proposes a simple evaluation method of the SAR antenna. The seven-panel antenna array performance is estimated from isolated single-panel antenna measurement results and synthesized scattering matrix. It is validated by comparing with near-field measurement of a seven-panel antenna array. The on-board SAR system is combined with a single-point source simulator and the point source SAR image is evaluated. The ambiguity to the signal ratio is computed for the bandwidth-integrated seven-panel antenna radiation patterns, and finally the pulse repetition frequency selection is computed along with noise equivalent sigma zero to estimate the SAR image quality based on various requirements of swath-width and ground-range resolution as per the application of interest. The prototype system is capable of 1-m ground-range resolution SAR image acquisition for 28-km swath-width within acceptable limits of signal-to-noise ratio and ambiguity levels.**

***Index Terms*—Ambiguity to signal ratio, earth observation, near-field measurement, noise equivalent sigma zero, pulse repetition frequency, remote sensing, scattering matrix, signal-to-noise ratio (SNR), slot array antenna, small satellite, synthetic aperture radar (SAR).**

I. Introduction

THE synthetic aperture radar (SAR) has several benefits for remote sensing applications compared to optical imagery like uninterrupted image acquisition even at night or during cloud cover. However, conventional SAR observation requires large or medium-size satellites weighing several hundred kilograms like TerraSAR-X [1] (Germany, total mass 1230 kg, 2007), SAR-Lupe [2] (Germany, total mass 770 kg, 2006), TecSAR [3] (Israel, 300 kg, 2008), and NovaSAR-S [4] (United Kingdom, 400 kg), which cost several hundred million USD including the launching cost. With rapid advancements in miniaturization of space technology, using SAR sensors on-board microsatellites in low earth orbits (LEO) with limited life span is becoming quite popular both for research and commercial applications: Synspective [5], Capella Space [6], Iceye [7], and IQPS [8] being some contemporary examples of future commercial LEO SAR constellations. For our MicroX-SAR mission, we have developed a 130 kg small satellite with on-board SAR sensor. It is capable of 3-m resolution SAR image acquisition in a strip-map mode and 1-m resolution SAR image acquisition in the sliding spotlight mode within acceptable noise equivalent sigma zero (NESZ) tradeoff. This article is an extension of [9], here a more detailed development of the antenna system is shown and SAR image performance metrices are calculated from the synthesized and measured antenna array radiation patterns to evaluate the scope of earth observation applications, which can be catered to by the mission.

Manuscript received February 28, 2020; revised May 21, 2020 and June 2, 2020; accepted June 28, 2020. Date of publication July 1, 2020; date of current version July 16, 2020. This work was supported by the Impulsing Paradigm Change through Disruptive Technologies Program (ImPaCT) of the Japan Science and Technology Agency (JST), Council of Science Technology and Innovation, Cabinet Office, Government of Japan. *(Corresponding author: Budhaditya Pyne.)*

Budhaditya Pyne and Prilando Riziki Akbar are with the Department of Satellite Systems Development, Synspective Inc., Tokyo 135-0022, Japan (e-mail: bupyn@synspective.com; akpri@synspective.com).

Hirobumi Saito, Jiro Hirokawa, and Takashi Tomura are with the Department of Electrical and Electronic Engineering, Tokyo Institute of Technology, Tokyo 152-8552, Japan (e-mail: fukami.tomoya@ac.jaxa.jphisai; jiro@antenna.ee.titech.ac.jp; tomura@ee.e.titech.ac.jp).

Koji Tanaka is with the Institute of Space and Astronautical Science (ISAS), Japan Aerospace Exploration Agency (JAXA), Sagamihara 252-5210, Japan (e-mail: tanaka.koji@jaxa.jp).

Digital Object Identifier 10.1109/JSTARS.2020.3006396

II. SAR System Development

In order to realize a compact SAR system compatible to 100-kg class satellite, unique SAR mission instruments have been developed. Fig. 1(a) shows the SAR system block diagram. The SAR system consists of SAR electrical processing unit (S-ELU) for transmitting signal generation and receiving signal processing, high-power amplifier (HPA) for signal transmission, SAR antenna, data recorder unit and data link, power supply system, and heat management system for the high-power amplifier. *X*-band SAR is advantageous to achieve high resolution with smaller satellite mass. Also, *X*-band is suitable for recognition of ground surface objects. Higher frequency bands than Ku band are subject to large rain attenuation. Furthermore, technology of GaN devices like high-power amplifiers is not well matured yet in higher frequency bands. Hence, *X*-band is selected for our mission. Table I describes the mission specifications. Transmission duty cycle 25% is relatively high to obtain high average TX power. From the standpoint of the TX amplifier, it is more difficult to increase its peak power than to increase its duty cycle when thermal management is properly applied. The system loss corresponds to the transmission loss inside the satellite from the *X*-band transmitter to the antenna input through the circulator and filter. The ohmic loss, dielectric loss, and reflection loss

TABLE I
MICROX-SAR MISSION SPECIFICATIONS

Parameter	Value
Antenna Size	4.9m x 0.7m
Desired Antenna Efficiency	> 50%
Ground-range Resolution	3m – 1m
Center Frequency	9.65GHz (X-band)
Frequency Bandwidth	100MHz – 300MHz
Swath-width	10km – 28km
Off-nadir Look Angle	15deg – 45deg
Satellite Altitude	510km (TBD)
Peak Power	1kW
Duty Cycle	25%
Pulse Repetition Frequency	3kHz – 6kHz
System Noise Figure	2.6dB
Ambient Temperature	290K
System Loss	0.55dB
Nadir Echo Duration Allowance	10μs
Guard Time Allowance	2μs
Azimuth Oversampling	1.33
Desired Mean NESZ	< –15dB
Desired Mean Ambiguity to Signal Ratio	< –17.5dB
Desired Max Antenna Reflection	< –15dB

inside the antenna are included in the antenna gain. The system noise figure corresponds to the cascaded noise figure from the antenna input to the low-noise amplifier (LNA) through the filter, circulator, and limiter including the noise figure of LNA when the antenna is facing toward the earth at 290 K noise temperature. This is described in Fig. 1(b).

A. SAR Antenna

From the considerations of wide bandwidth with low reflection loss, low-cost, light-weight, and simple fabrication for mass production, a passive honeycomb panel slot-array antenna with a waveguide feeder network system was selected [10]–[14]. The following Sections II-A.1 and II-A.2, respectively, provide an overview of the antenna system architecture and detailed analysis of the antenna array performance evaluation from single-panel measurement results.

1) Antenna System Architecture: Fig. 2 shows the configuration of SAR antenna. "M" and "P" denote the negative and positive sides w.r.t the satellite body y-axis. Each panel is 70 × 70 cm in size, and the antenna size in deployed condition is 4.9 × 0.7 m, which in stowed condition prelaunch can be fit into a 0.7 × 0.7 × 0.7 m satellite body. The waveguide is embedded at the center of the rear surface in order to feed RF to the antenna panel through coupling slots. The antenna panel consists of a dielectric

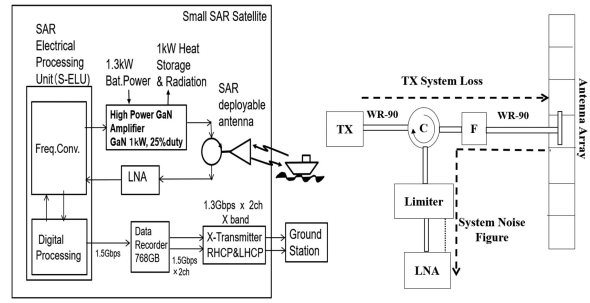

(a) (b)

Fig. 1. (a) MicroX-SAR system block diagram. (b) Noise figure and system loss overview.

honeycomb core and metal skins, which function as a parallel plate guide for RF. The front surface with 2-D arrays of radiation slots works as an antenna radiator for the vertical polarization SAR mode. The layered antenna structure is explained in detail in [14], where the engineering model measurement results are shown, and an undesired high reflection level is observed due to mismatch in the adhesive layer thickness. In the present state, this problem has been compensated by increasing the length of all coupling slots in the waveguide feeders of engineering model by 0.2 mm, and new flight model antenna panels have been fabricated. In the deployed condition, RF power is fed between adjacent panels through a contactless choke flange with a nominal airgap of 0.9 mm to prevent corrosion from thermal expansion in space. The shape of choke is designed in such a way which ensures that standing waves are not excited at the region between the waveguide aperture and the choke groove in the frequency band of interest, considering possible misalignments between the connecting joints during practical operation. For our mission, an egg-shaped choke flange was designed for wideband applications in X-band from 8.5 to 11 GHz [15].

2) Single-Panel Antenna Measurement Results and Seven-Panel Pattern Synthesis Using Cascaded Scattering Matrix: Fig. 3(a)–(b) shows the block diagram of the antenna network for estimation of the full system performance from isolated single-panel measurements. Fig. 3(c)–(d) shows the antenna waveguide feeder network and fabricated flight model antenna panels, respectively. The P-side and M-side are symmetric, i.e., for example, panels 1P and 1M must have identical design. The center panel #0 on the satellite body has two input ports that must be fed symmetrically, i.e., panels 1P and 1M must have identical design. Panels #1, #2, and #3 include a τ-junction and comprise of 3 ports, 2 ports, and 1 port, respectively. Panel #2 has one additional layer of τ-junction (without coupling slots), which functions as a simple 1:1 power divider. Port 2 of panel #2 feeds panel #3. panel #1 has two additional layers of τ-junctions (without coupling slots), which function as a power divider with dividing ratios 2:1 and 4:3, respectively. Ports 2 and 3 of panel #1 feed panel #2 and panel #0, respectively. These upper layer power divider τ-junctions cannot be placed at the center between two adjacent panels due to the presence of the choke flange. Thus, they must be shifted such that the path difference of either

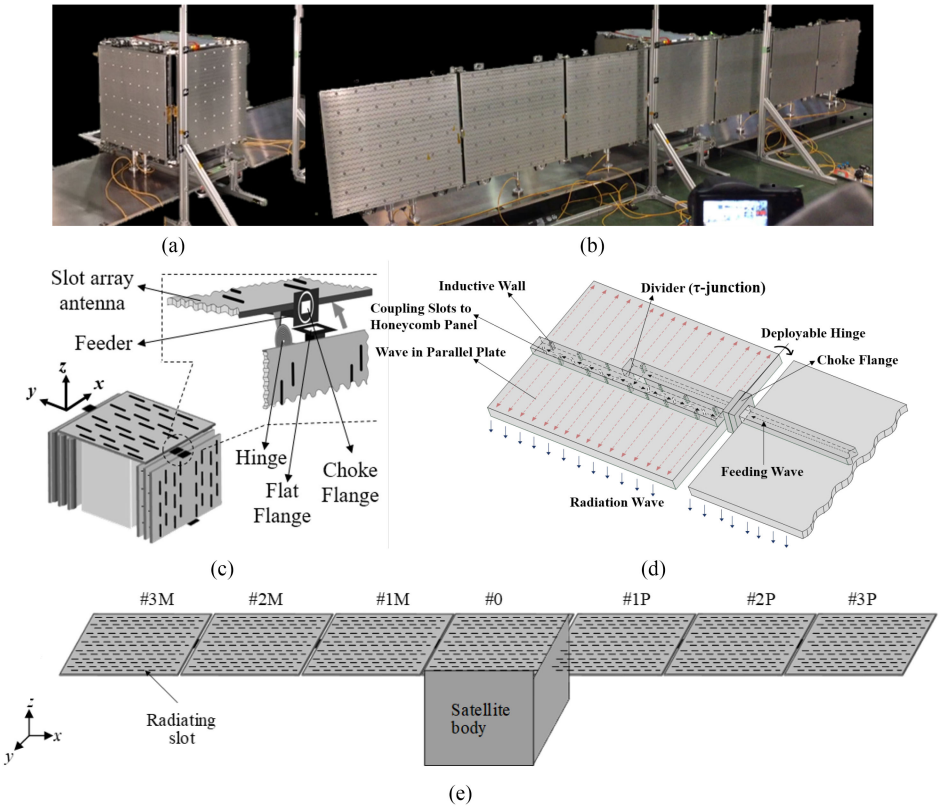

Fig. 2. MicroX-SAR antenna system overview. (a) Stowed configuration prelaunch. (b) Deployed configuration. (c) Noncontact waveguide feeding with choke flange. (d) Honeycomb antenna panel with slot-array and embedded waveguide. (e) Antenna panel nomenclature in deployed configuration.

branch of the tournament circuit is an integral multiple of the wavelength at the center frequency in order to ensure in-phase excitation of all panels [14].

Isolated single-panel measurements were performed at a near-field measurement anechoic chamber in ISAS, JAXA using x-y scanner. The open-end waveguide (OEWG) WR90 probe was placed at a height of 15 cm from the AUT and sampling was done at a spacing of 15 mm in both x and y directions, covering 75×75 data points to satisfy the Nyquist sampling criterion. It is to be noted that to perform array synthesis, the VNA calibration prior to the near-field measurement is important since the absolute phase is important for synthesis. The absolute phase is likely to change due to day-to-day variation and change in the shape of RF coaxial cable. Thus, VNA calibration is done prior to the measurement of each panel and probe correction is also applied. For Panel #0, power was fed from the VNA to Port 1 and Port 2 through a 1:1 Wilkinson power divider with phase shifter as explained in [14]. The phase shifter was adjusted so that the signal at port 1 and port 2 had a uniform amplitude and same phase. For Panel #1, power was fed from the VNA to Port 1. Port 2 and Port 3 were terminated by matched load. For Panel #2, power was fed from the VNA to Port 1. Port 2 was terminated by matched load. For panel #3, power was fed from the VNA to Port 1. The 2×2, 2×2, 3×3, and 1×1 scattering matrices coefficients for panels #0, #1, #2 and #3, respectively, were separately measured with VNA calibration. For Panel #0, the active reflection coefficients were computed.

Fig. 4(a) shows the aperture distribution of amplitude and phase from the near-field measurement at the center frequency. The phase of panels #0, #1, and #2 includes the phase of the upper layer τ-junctions part of the waveguide feeder tournament circuit. Thus, as per design, the radiation phase of each panel is different. However, the radiation phase of the P-side and M-side should be same. Fig. 4(b)–(c) shows the converted far-field radiation patterns at the center frequency, Fig. 4(d) shows the variation of peak directivity with frequency. The peak aperture efficiency (without considering antenna loss) and peak antenna efficiency (considering antenna loss) of single-panel antenna (e.g., #3M) are 65.6% and 53%, respectively. Fig. 4(e)–(f) shows the measured scattering matrix transmission amplitude and transmission phase, respectively. The desired amplitude is obtained from the theoretical design goal and the desired phase is obtained from HFSS simulation results based on design. Fig. 4(g) shows the measured scattering matrix reflection level.

Although the size of each panel is 70 cm $\times$ 70 cm, the total length of the antenna in azimuth is 4.9 m in the deployed configuration. There are only a few test facilities that are large enough to enable near-field measurement of such a long antenna. Furthermore, they are expensive to use and not readily accessible. Thus, accurate synthesis from single-panel measurement becomes important for a low-cost SAR satellite.

Synthesis is done utilizing the measured antenna scattering matrix coefficients in the far-field with the approximation that each antenna panel can be represented as a point element located

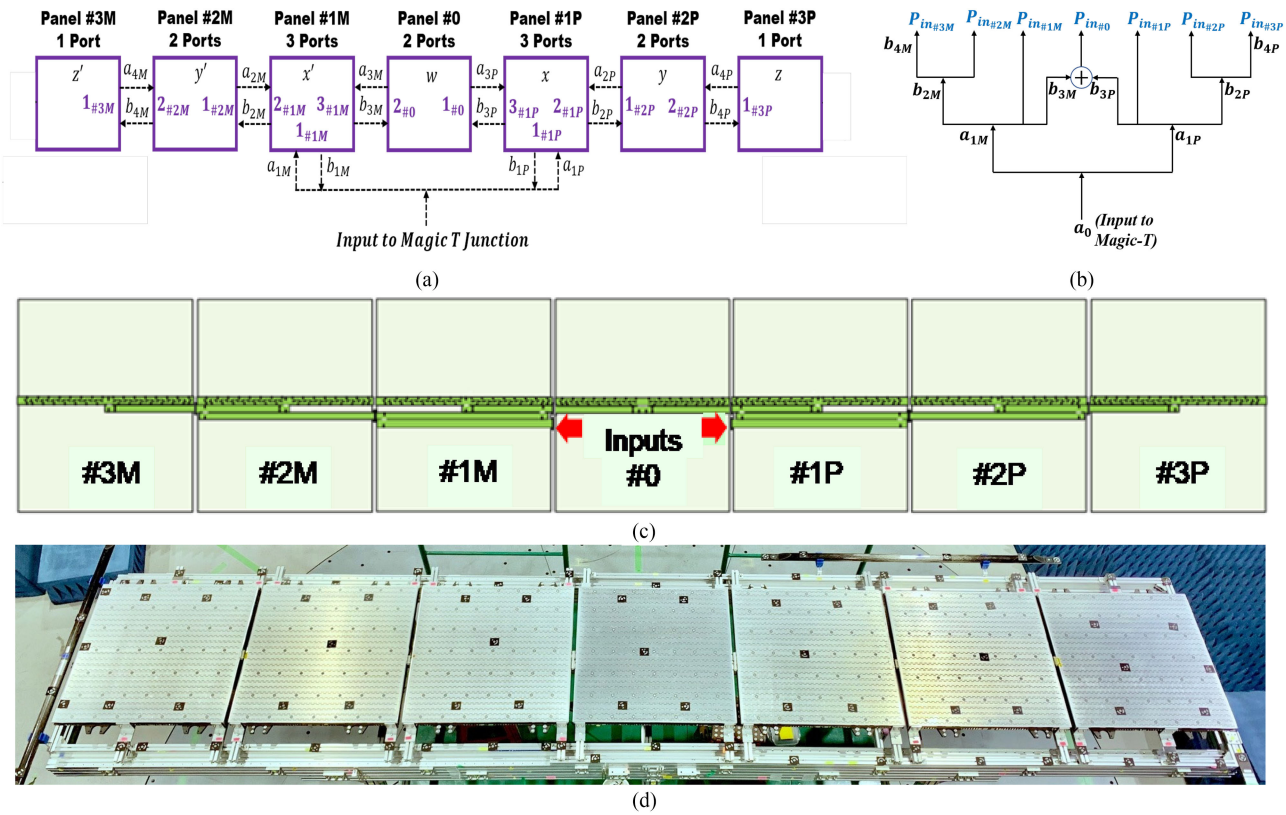

Fig. 3. MicroX-SAR antenna array network block diagram. (b) Power feeding network overview. (c) Waveguide feeder network. (d) Fabricated 4.9 × 0.7 m seven-panel flight model antenna array.

at the center of the panel as follows [see Fig. 3(a) and (b)]:

$$E_{\mathrm{az7-panels}}\ (\theta_{\mathrm{az}}) = \sum_{n=-3}^{3} \mathrm{E}_{\#\mathrm{az_n}} e^{-jkd_{\#n}\mathrm{Sin}(\theta_{\mathrm{az}})} \tag{1}$$

$$\mathrm{E}_{\#\mathrm{az_n}} = \sqrt{\mathrm{P_{in\#n}}}\, e^{-j\varphi_{in_{\#n}}} \sqrt{\mathrm{Dir}_{\#\mathrm{az_n}}} e^{-j\varphi_{az_{\#n}}} \quad -3 \le n \le 3 \tag{2}$$

$$d_{\#n} = X_{c_{\#n}} + n\delta_{\mathrm{gap}} \quad -3 \le n \le 3\ n \neq 0\ \ d_{\#0} = 0 \tag{3}$$

$$P_{in_{\#0}} = |b_{3M}|^2 + |b_{3P}|^2,\ \ \varphi_{in_{\#0}} = \frac{1}{2}\left(\angle b_{3M} + \angle b_{3P}\right) \tag{4}$$

$$P_{in_{\#1}} = |a_1|^2 - |b_2|^2 - |b_3|^2,\ \ \varphi_{in_{\#1}} = \angle a_1 \tag{5}$$

$$P_{in_{\#2}} = |b_2|^2 - |b_4|^2,\ \ \varphi_{in_{\#2}} = \angle b_2 \tag{6}$$

$$P_{in_{\#3}} = |b_4|^2,\ \ \varphi_{in_{\#3}} = \angle b_4 \tag{7}$$

$$b_2 \approx S_{21_{\#1}} a_1,\ b_3 \approx S_{31_{\#1}} a_1,\ b_4 \approx S_{21_{\#2}} b_2\ . \tag{8}$$

Here, $E_{\mathrm{az7-panels}}$ is the seven-panel synthesized radiation field in azimuth direction, $E_{\#az_n}$ is the effective field of isolated panel "n" at the origin, $\mathrm{Dir}_{\#az_n}$ and $\varphi_{az_{\#n}}$ are the far-field radiation power and phase in the azimuth cut of the isolated panel "n" at the origin, respectively. This is obtained from Fig. 4(c). The center of panel #0 is considered as the reference point or phase center of synthesis, $X_{c_{\#n}}$ is the distance of the center of each panel from the center of panel #0 without any air-gap between adjacent panels, $d_{\#n}$ is the equivalent distance of the center of each panel from the phase center. δ_{gap} is the nominal air-gap of 0.9 mm between each pair of adjacent choke-flange and flat-flange to prevent thermal corrosion. $P_{in_{\#n}}$ is the power fed into panel "n" through the Magic-T junction and can be computed from Fig. 3(b), which shows the power feeding network. $\varphi_{in_{\#n}}$ is the phase of the input signal to port 1 of each panel and can be computed in terms of the cascaded scattering matrix coefficients a_n and b_n. It is to be noted that since a_n and b_n are computed utilizing the results from Fig. 4(e)–(g). Here, also the absolute phase of the scattering matrix coefficients are necessary, and hence, VNA calibration prior to scattering matrix measurement of each panel is necessary. Power is fed through the radar front end (RFE) into the Magic-T, which functions as a 1:1 power divider to feed panel #1 on the P-side and M-side. Thus, $|a_{1M}|^2 = |a_{1P}|^2 = \frac{1}{2}$ and $\angle a_{1M} = \angle a_{1P} = 0$ (normalized as reference phase). b_2 and b_4 are the input signals to port 1 of panels #2 and #3, respectively. b_1, a_2, a_3, and a_4 are the return signals arriving at port 1 of panels #1, #2, #0, and #3, respectively, due to reflection. Since the reflection level is quite low, (8) is a good approximation and it reduces the computation burden.

For ideal uniform in-phase excitation, the input power to each panel must be equal and far-field power and phase of each panel in the normal direction ($\theta_{\mathrm{az}} = 0$, $\theta_{\mathrm{el}} = 0$) must be equal, where θ_{az} and θ_{el} are the radiation pattern angles in the azimuth cut plane and elevation cut plane, respectively. Thus, the following condition must be satisfied as per design and HFSS simulation

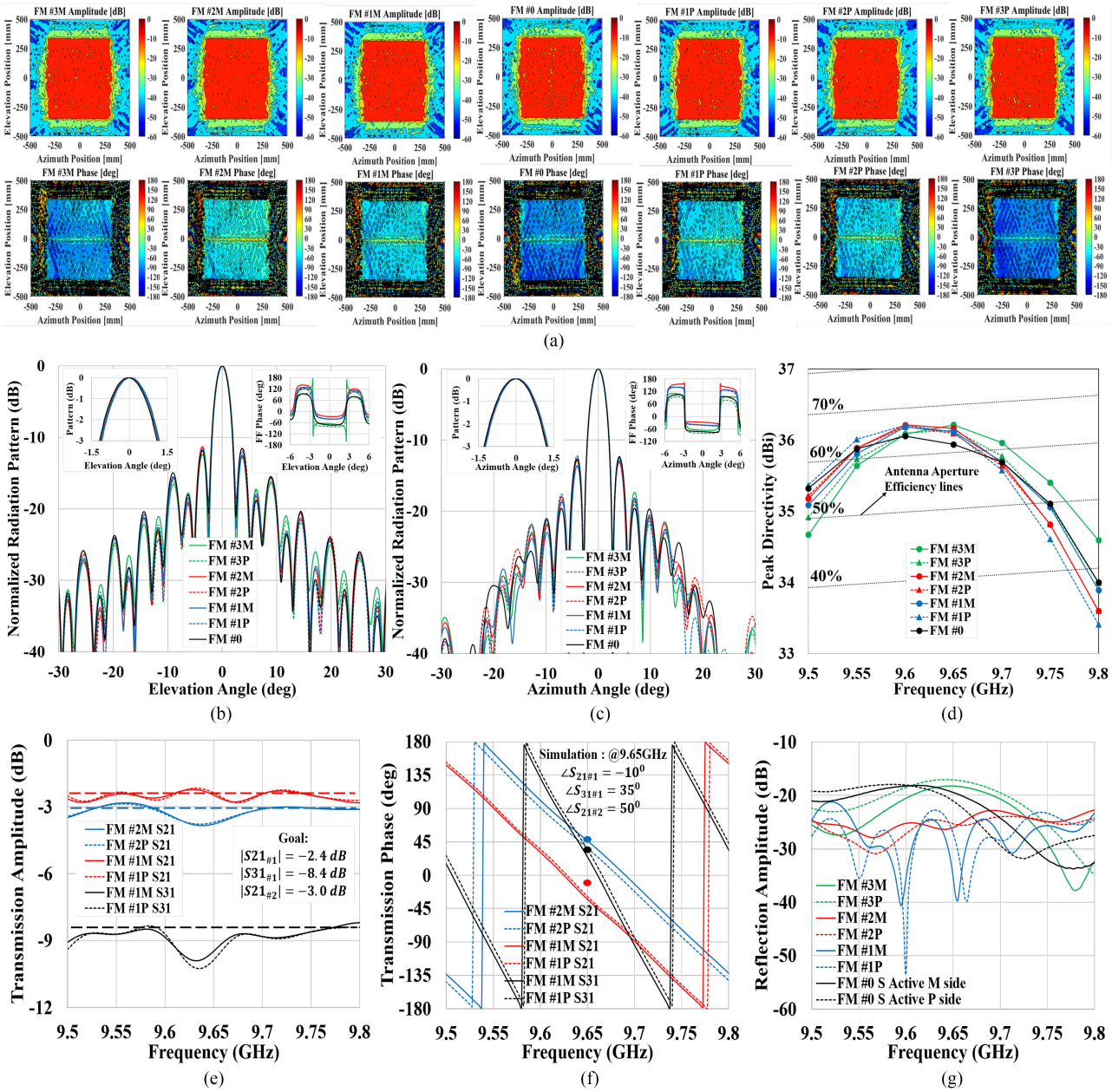

Fig. 4. Isolated single-panel near-field measurement results. (a) Aperture distribution amplitude and phase at 9.65 GHz. (b) Radiation pattern in elevation cut-plane at 9.65 GHz. (c) Radiation pattern in azimuth cut-plane at 9.65 GHz. (d) Peak directivity versus frequency. (e) Scattering matrix transmission amplitude. Dotted lines show the goal values. (f) Scattering matrix transmission phase. Solid circles show the phase from HFSS simulation. (g) Scattering matrix reflection level.

at 9.65 GHz:

$$\varphi_{eq_{\#n|\ \theta_{\mathrm{az}}=\ 0}} = \varphi_{in_{\#n}} + \varphi_{az_{\#n|\ \theta_{\mathrm{az}}=\ 0}} = \text{const.},\ -3 \le n \le 3 \tag{9}$$

$$P_{in_{\#n}} = \frac{1}{7}\ ,\ \mathrm{Di\,r}_{\#az_{n|\ \theta_{\mathrm{az}}=\ 0}} = \text{const.},\ -3 \le n \le 3\ . \tag{10}$$

However, due to fabrication imperfections (i.e., variation from designed value of some uncontrollable antenna parameters like adhesive permittivity, adhesive thickness, honeycomb permittivity, WR90 feeder dimensions, etc.), thus, uniform in-phase excitation of all panels cannot be perfectly achieved as listed in Table II. Panel #0 has the maximum difference of –1.12 dB in the power level from the desired –8.45 dB, and the maximum phase deviation of –36° occurs at the far-field between panels 1M and 3P. Furthermore, there is a deviation from the symmetricity prerequisite between the M-side and the P-side. Fig. 5(a) and (b) shows that the cascaded scattering matrix transmission amplitude and transmission phase is approximately symmetric. The desired amplitude is obtained from the theoretical design goal, and the desired phase is obtained from HFSS simulation results based on design. This shows that the waveguide tournament circuit is symmetric. However, it is seen that the far-field phase for the panels is not symmetric, for, e.g., there exists 15° phase

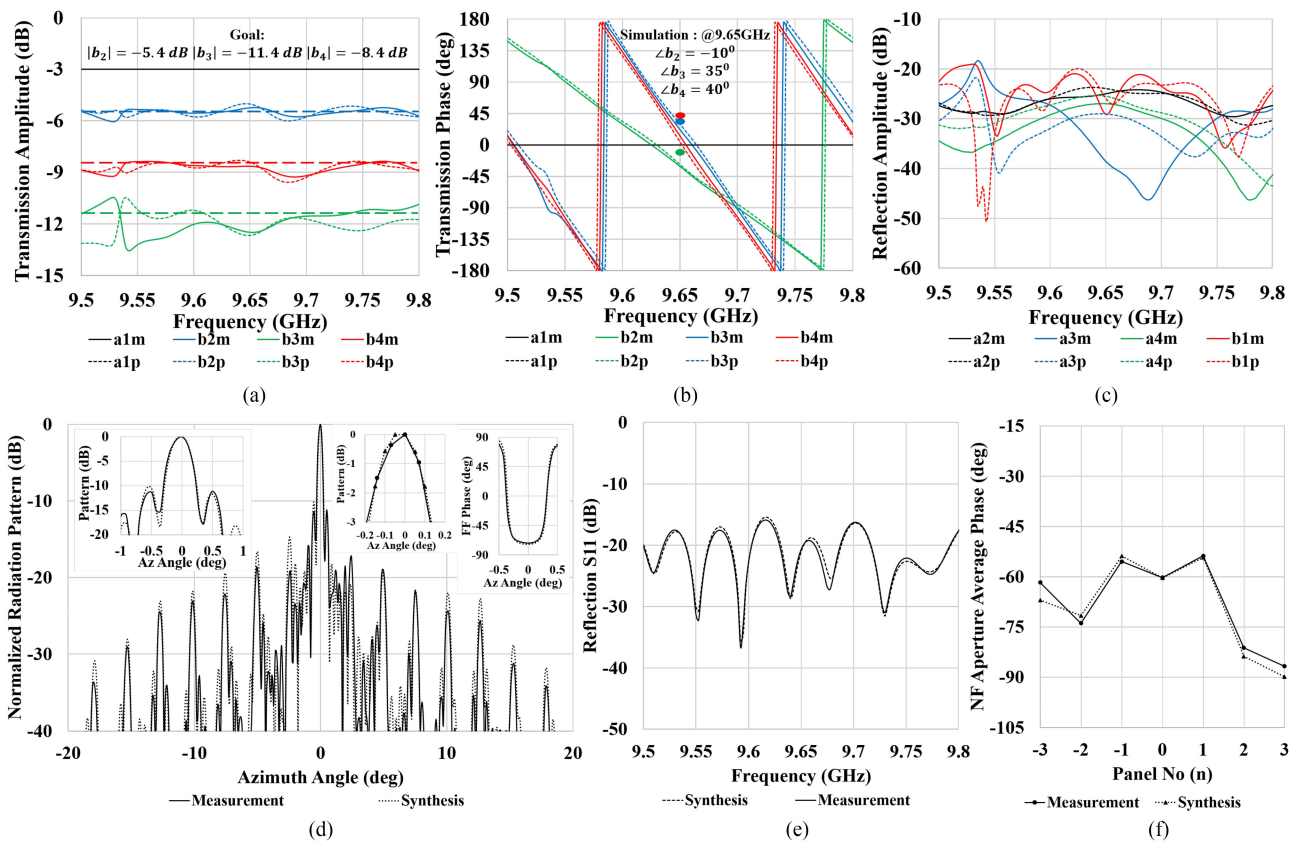

Fig. 5. (a) Synthesized scattering matrix transmission amplitude. Dotted lines show the goal values. (b) Synthesized scattering matrix transmission phase. Solid circles show phases from HFSS simulation. (c) Synthesized scattering matrix reflection amplitude. (d) Synthesized and measured seven-panel array azimuth pattern at 9.65 GHz. (e) Synthesized and measured seven-panel array system reflection. (f) Synthesized and measured seven-panel array near-field average phase.

TABLE II
SYNTHESIZED INPUT SIGNAL POWER AND PHASE TO EACH PANEL IN SEVEN-PANEL ARRAY AT 9.65 GHZ

Panel No (n)	$P_{in_{\#n}}$ (dB)	$\varphi_{az_{\#n\|\theta_{az}=0}}$ (deg)	$\varphi_{in_{\#n}}$ (deg)	$\varphi_{eq_{\#n\|\theta_{az}=0}}$ (deg)
-3	-8.66	-66.57	12.56	-54.01
-2	-7.89	-27.84	-30.71	-58.55
-1	-8.39	-40.85	0	-40.85
0	-9.57	-73.13	25.86	-47.28
1	-8.82	-41.26	0	-41.26
2	-7.69	-42.87	-27.94	-70.81
3	-8.4	-81.31	4.44	-76.87

difference between panels 3M and 3P and between panels 2M and 2P in Fig. 4(c). This radiation phase asymmetry is the main cause behind the cascaded phase asymmetry observed in Table II and Fig. 5(f), which shows the near-field aperture distribution average phase of each panel. Since the honeycomb panel and radiation slots design are identical for all panels, this asymmetry is unexpected and can be attributed to fabrication imperfections discussed earlier. One possible way to compensate this phase imbalance for future satellites is to adjust the air-gap between adjacent panels in the M-side and P-side accordingly.

The total system reflection can be estimated from the single-panel measured scattering matrix as follows:

$$\begin{aligned} S_{11_{7-\text{Panels}}} = {} & S_{11_{Tj}} + S_{21_{Tj}} S_{31_x} S_{1\text{Active}_w} S_{13_x} S_{12_{Tj}} \\ & + S_{21_{Tj}} S_{11_x} S_{12_{Tj}} + S_{21_{Tj}} S_{21_x} S_{11_y} S_{12_x} S_{12_{Tj}} \\ & + S_{21_{Tj}} S_{21_x} S_{21_y} S_{11_z} S_{12_y} S_{12_x} S_{12_{Tj}} \\ & + S_{31_{Tj}} S_{31_{x'}} S_{2\text{Active}_w} S_{13_{x'}} S_{13_{Tj}} \\ & + S_{31_{Tj}} S_{11_{x'}} S_{13_{Tj}} + S_{31_{Tj}} S_{21_{x'}} S_{11_{y'}} S_{12_{x'}} S_{13_{Tj}} \\ & + S_{31_{Tj}} S_{21_{x'}} S_{21_{y'}} S_{11_{z'}} S_{12_{y'}} S_{12_{x'}} S_{13_{Tj}}. \end{aligned} \quad (11)$$

Here subscript "Tj" refers to the Magic-T junction, x, y, z and x', y', z' refer to panels 1,2,3 on the P-side and M-side, respectively, "w" refers to panel #0, which has two input ports; hence, S-active must be considered.

Fig. 5(c) shows the cascaded scattering matrix reflection level. In order to validate this synthesis methodology and thereby judge its accuracy level, it is necessary to compare the synthesis results with actual measurement results. The seven-panel near-field measurement was conducted at AMETLAB NSI-MI plane-polar measurement facility at Kyoto University Uji Campus. As shown in Fig. 6(a), a lift-up table is employed to fix the distance between the AUT and the log-peri antenna probe to 5λ, where λ is the wavelength at the center frequency. The radial span is

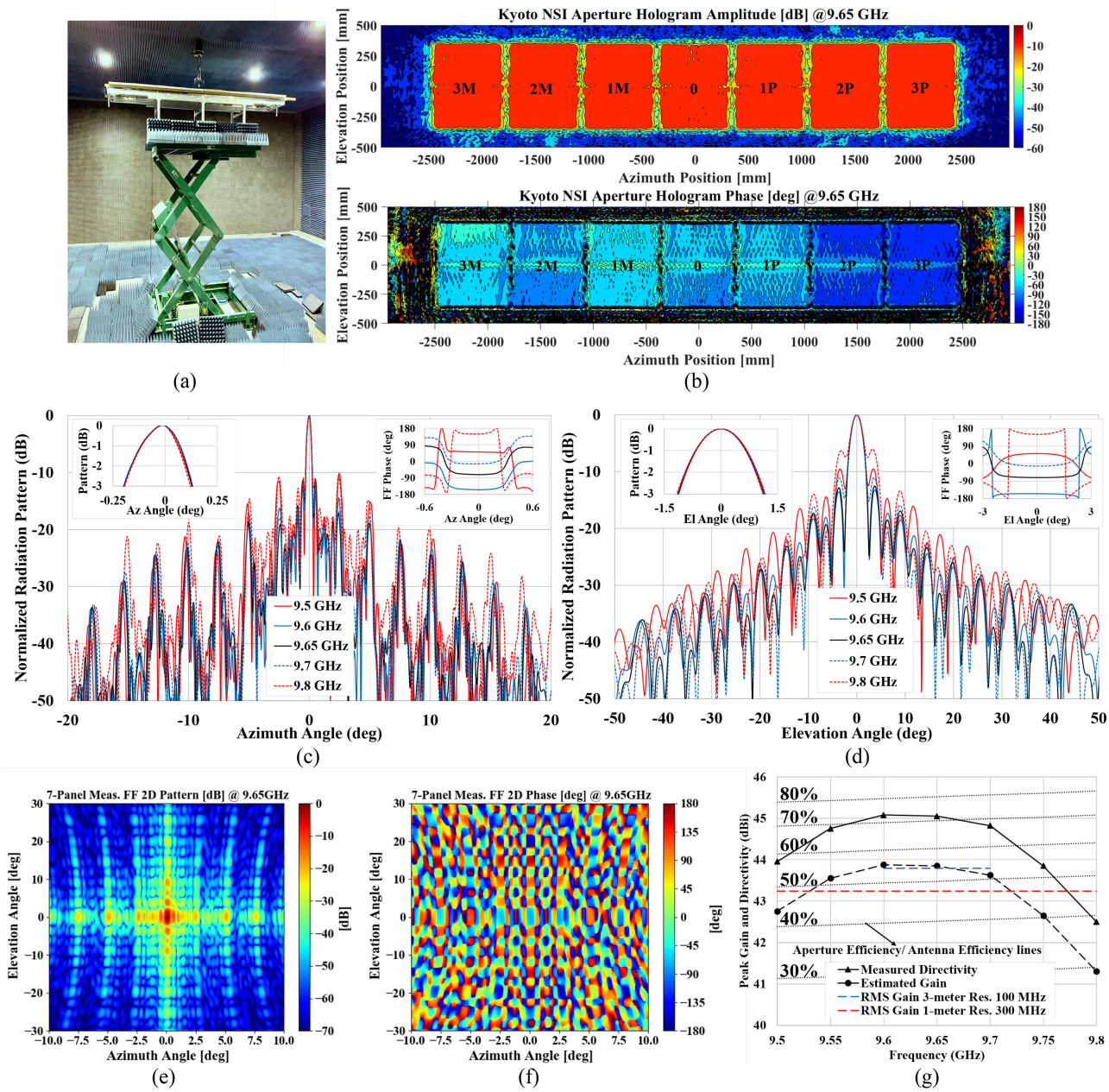

Fig. 6. Seven-panel array near-field measurement. (a) Setup. (b) Aperture distribution amplitude and phase at 9.65 GHz. (c). Frequency-dependent azimuth pattern. (d) Frequency-dependent elevation pattern. (e) 2-D radiation pattern amplitude at 9.65 GHz. (f) 2-D radiation pattern phase at 9.65 GHz. (g) Variation of peak directivity and estimated peak gain with frequency.

5902.23 mm, and the sampling is done at a spacing of 14.47 mm in radial direction and 0.29° in the angular direction, thereby covering 409 × 626 2-D radial data points, which meet the Nyquist sampling criterion. Log-peri probe correction is not considered in the NSI-MI near-field measurement software.

Fig. 6(b) shows the near-field measurement aperture amplitude and phase distributions. Fig. 5(d) shows the transformed far-field azimuth pattern at the center frequency. The azimuth pattern is asymmetric due to the asymmetric phase imbalance observed in Fig. 5(f). Fig. 5(e) shows the system reflection. In all cases, it is seen that there is a good match between the synthesized patterns and the measurement patterns. A constant phase offset due to no calibration of the VNA before seven-panel measurement has been compensated for the sake of comparison. The error in average phase estimation is less than 5°. The main beam far-field phase, 3 dB beamwidth, and first sidelobe level match quite well; and the same applies for the system reflection level. The 3 dB beamwidth of the synthesized and measured pattern are, respectively, 0.3° and 0.28°. The first sidelobe levels (SLL) of the synthesized pattern are –10.2 and –11.7 dB while that of the measured patterns are, respectively, –11.4 and –11.2 dB, respectively. Thus, the 3 dB beamwidth error is 0.02°, i.e., 7.1%; and the first SLL errors are 1.2 and –0.5 dB, respectively, i.e., 14.8% and –5.6% w.r.t. the field

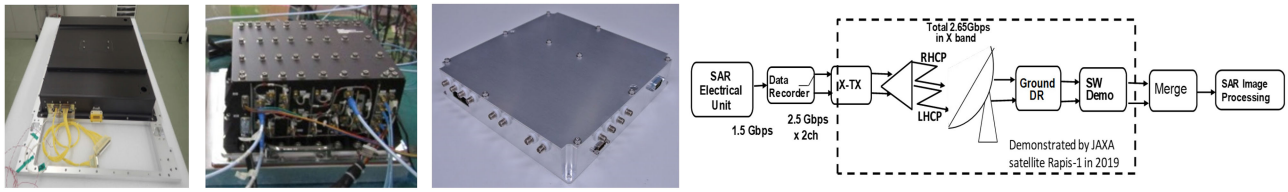

(a) (b) (c) (d)

Fig. 7. (a) *X*-band HPA installed on the satellite body panel. (b) SAR S-ELU converted from airplane application. (c) MDR with 768 GB NAND flash memory. (d) System block diagram of SAR data storage and downlink system.

strength magnitudes. Some larger discrepancies between measurement and synthesis are seen in the azimuth pattern at far angles. However, since the azimuth beamwidth is very narrow, the sidelobes at these far-angles are well below –15 dB and, hence, have minimal influence on the system performance. Thus, these errors are within acceptable limits from the perspective of system performance evaluation. The most likely cause behind these discrepancies is that the isolated single-panel near-field measurement (and hence synthesis pattern) was performed with OEWG probe including the effect of probe correction and after near-field to far-field transformation, the angle resolution is 0.5°. In contrast, the seven-panel measurement was conducted with log-peri probe without considering the effect of probe correction, and the corresponding far-field angle resolution is 0.7°. An additional minor factor is that the measurement scan area of single panel is much narrower than the seven-panel array. The system reflection is also critical since high reflection can damage the LNA. Maximum reflection level less than –15 dB is achieved as desired. These are the primary parameters of interest for synthesis, since the main lobe beamwidth and the first sidelobe levels determine the SAR azimuth ambiguity level, which will be discussed in the following section. This validates the synthesis results and methodology and confirms that the approximations in (8) and (11) are acceptable.

Fig. 6(g) shows the variation of measured peak directivity and estimated peak gain with frequency. The gain is estimated assuming a constant antenna loss of 1.2 dB, throughout the bandwidth, this antenna loss is estimated using the measured antenna loss of a single-panel engineering model antenna far-field measurement in [14]. A traveling wave antenna is designed for in-phase excitation at the center frequency; thus, it is expected that the gain will drop at the edge frequencies; the drop in the gain becomes more pronounced at one of the edge frequencies if the center frequency shifts. The directivity drops more sharply at a higher frequency since the measured center frequency is shifted to 9.62 GHz from 9.65 GHz. At 9.65 GHz, the aperture efficiency and estimated antenna efficiency (including 1.2 dB antenna loss) are, respectively, 73% and 55%. The arraying efficiency, i.e., ratio of seven-panel measured directivity w.r.t ideal uniform in-phase excitation of seven identical panels (considering isolated single-panel #3P measured directivity) is 94.2%. Fig. 6(c) and (d) shows the seven-panel measurement radiation patterns along azimuth and elevation, respectively, throughout the designed bandwidth of 9.5–9.8 GHz. Fig. 6(e) and (f) shows the 2-D far-field radiation pattern amplitude and phase, respectively, at 9.65 GHz. The azimuth pattern at 9.65 GHz has slightly higher sidelobes of –11.2 dB and the pattern is not perfectly symmetric. This is a consequence of the deviation from ideal uniform in-phase feeding condition described in Table II causing phase-imbalance in the near-field distribution between adjacent panels shown in Fig. 5(f). It is also seen that radiation patterns have higher sidelobes at 9.8 GHz, especially in elevation. This is due to the shift of the center frequency to 9.62 GHz from designed 9.65 GHz due to fabrication imperfection discussed earlier.

B. On-Board SAR Electronics

This section explains the on-board SAR instruments, the high-power amplifier, S-ELU, mission data recorder, and the data downlink system. Fig. 7(a)–(c) shows the on-board SAR instruments. Fig. 7(d) shows the system block diagram of data storage and downlink system.

The RF peak power is selected to be 1000 W that is realized by GaN solid-state amplifiers, instead of vacuum tube TWTAs. The on-duty ratio is selected as 25% to increase the average transmitting power, paying careful attention to the thermal design [16].

A chirped transmitting signal is amplified in 6 GaN HEMT 200 W amplifier modules to be combined in a waveguide resonator. The inputs of the power combiner are microstrip lines. The output of the combiner is a rectangular waveguide. Total heat generation of the HPA is about 1000 W in average. The duration of SAR observation is less than 5 min per one orbit period (96 min). Six amplifier modules are distributed around the power combiner and are fastened almost directly to the satellite structural panel. The structural panel is a thick aluminum plate that works as a heat spreader, heat capacitor, and radiator. Aluminum has relatively high specific heat (0.9 kJ/K/kg) and thermal conductance (200 W/K/m). The mass of the aluminum plate is about 4.4 kg and the temperature of the plate rises by 50° after 5 min of SAR observation. The heat stored in the aluminum plate during SAR observation is emitted with a time constant of about 50 min as infrared radiation from an outer radiator surface of the aluminum plate to deep space.

A S-ELU handles transmitting signal generation, receiving signal processing (frequency conversion and analog-to-digital conversion) for the SAR sensor. The S-ELU for our small satellite is developed based on an airborne SAR instrument. The chirp bandwidth is 300 MHz for 1-m ground resolution. The received

signal is converted to digital signal of 8 b × 720 Mega-samples/s. The data compression rate is about 50%. Receiving duty cycle is about 50% to acquire a reasonable signal-to-noise ratio. After the time stretching process, the average data rate is 1.5 Gigabit/s.

SAR data are transferred to MDR through serial RapidIO (sRIO) interface. The MDR consists of commercial 16 NAND flash memory devices and the total memory capacity is 768 GB. Total dose tolerance of NAND devices is confirmed by the Co60 irradiation test. Single event upset errors are corrected by a standard error correction code for commercial NAND devices. A commercial Xilinx ultrascale FPGA (field programmable gate array) device is utilized for high-speed data flow and standard powerful error correction code. Special care is given to thermal heat path and thermal stress of ball brid array (BGA) packaging.

In the downlink communication mode, the stored data are transferred to a high data rate *X*-band transmitter (XTX). XTX has dual polarization (RHCP/LHCP) channels to increase its downlink capability. The stored data are switched to the two channels and they are transferred to XTX through Xilinx Aurora data interface. The data rate between MDR and XTX is 2 Gigabits/s per one channel and total data rate is 4 Gigabits/s. The downlink system is demonstrated by JAXA Rapis-1 satellite in 2019 [22].

III. SAR System Evaluation

A. SAR Imaging Test With Point Source Simulator

Ground test of SAR observation has been performed with a dedicated target signal simulator. Prototype flight model viz. PFM of S-ELU sends exciter signal with chirp modulation to radar front-end (RFE) and HPA. A dedicated target signal generator generates echo signals from a single-point target under assumption of the stop and go model. The echo signals are input to S-ELU. Then S-ELU performs frequency down-conversion, conversion of analog signal to digital signal, and data compression. Then the observation data are sent to the MDR. Based on the stored data, conventional SAR image processing generates the range-azimuthal SAR image of a point target, as shown in Fig. 8. A 0.81-m azimuthal resolution and 0.86-m ground-range resolution at the 30° off-nadir angle in the sliding spotlight mode has been confirmed.

B. SAR Image Quality Evaluation

In this section, SAR image quality evaluation is performed for strip-map mode operation with 2.45-m azimuthal resolution. The three key SAR image quality indices that can be estimated from the measured seven-panel array antenna pattern are NESZ, range ambiguity to signal ratio (RASR), and azimuth ambiguity to signal ratio (AASR) as follows [17]:

$$\sigma_{\mathrm{NEZ0}} = \frac{8\pi R^3 \lambda V L_R k T_0 N_F}{P_t G_{\max}^2 \delta_{\mathrm{gr}} D_p} \tag{12}$$

$$\mathrm{AASR} = \frac{\sum_{n=-\infty}^{\infty} \int_{-\frac{B_P}{2}}^{\frac{B_P}{2}} G_{\mathrm{az}}^2 \left(f_d + n f_p\right) df_d}{\int_{-\frac{B_P}{2}}^{\frac{B_P}{2}} G_{\mathrm{az}}^2 \left(f_d\right) df_d}$$

$$n = \pm 1, \pm 2.. \neq 0 \tag{13}$$

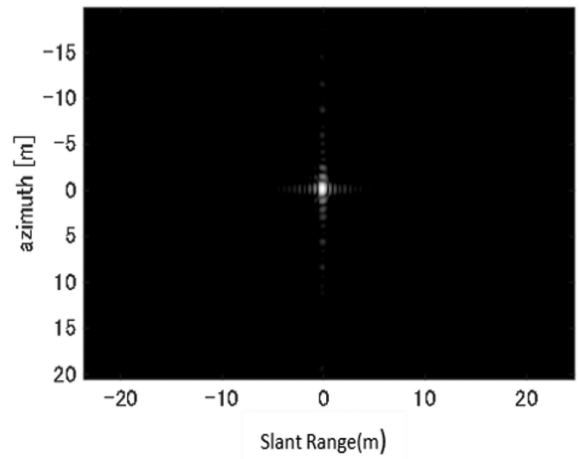

Fig. 8. SAR response image of single-point source with a sliding spotlight mode. 2-D plot of slant range and azimuthal direction. Azimuthal resolution is 0.81 m. Slant range resolution is 0.47 m. Ground range resolution 0.86 m at 30° look angle

$$\mathrm{RASR} = \frac{\sum_{n=-\infty}^{\infty} \sum_{t_i}^{t_f} X_{\mathrm{el}} \left(t + \frac{n}{f_p}\right)}{\sum_{t_i}^{t_f} X_{\mathrm{el}} \left(t\right)}$$

$$n = \pm 1, \pm 2.., \neq 0 \ (14) \tag{14}$$

$$f_d = \frac{2V}{\lambda} \sin\theta_{\mathrm{az}}, \ \ B_P = \eta \frac{2V}{L_{\mathrm{az}}}, \ 0 < \eta \leq 1 \tag{15}$$

$$\cos\gamma = \frac{(R_e + h)^2 + R^2 - R_e^2}{2R\left(R_e + h\right)}, \ \sin\theta_i = \left(1 + \frac{h}{R_e}\right) \sin\gamma \tag{16}$$

$$X_{\mathrm{el}} = \frac{G_{\mathrm{el}}^2}{R^3 \sin\theta_i}, \ t = \frac{2R}{c}, \ \gamma = \gamma_0 + \theta_{\mathrm{el}} \tag{17}$$

$$\mathrm{S\ W}_i = R_e \ (\alpha_f - \alpha_n) \tag{18}$$

$$\beta_i = \gamma_f - \gamma_n. \tag{19}$$

Here, P_t is the peak transmission power, $G_{\max}$ is the peak gain, D_p is the duty cycle, δ_{gr} is the ground-range resolution, R is the slant range, λ is the wavelength, V is the satellite orbital velocity, L_{az} is the antenna length in azimuth, L_R is the system loss, k is Boltzmann's constant, T_0 is the ambient noise temperature, B_P is the azimuth processing bandwidth. η determines how much the processing bandwidth is utilized, and $\eta < 1$ corresponds to oversampling w.r.t. the Nyquist rate. These parameters are listed in Table I. Typically, $\eta = 0.75$, which corresponds to an azimuth oversampling of 1.33, i.e., the azimuth processing bandwidth is greater than the Doppler bandwidth $\frac{2V}{L_{\mathrm{az}}}$. G_{az} is the antenna radiation pattern in the azimuth cut plane, θ_{az} is the azimuth angle, f_d is the Doppler frequency, f_p is the pulse repetition frequency (PRF). Referring to Fig. 9, γ is the look angle, γ_0 is the nadir offset angle at elevation beam-center, G_{el} is the antenna radiation pattern in the elevation cut plane, θ_{el} is elevation angle, θ_i is the angle of incidence, α is the core angle, h is the satellite altitude, R_e is the radius of the earth, R is the slant-range, t is the time, and c is the speed of light in free space, t_i and t_f correspond to the receiving window echo reception from the near-range and far-range, respectively.

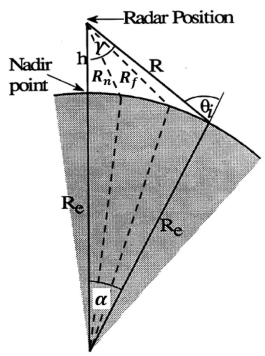

Fig. 9. SAR geometry assuming spherical earth [17].

The antenna pattern is a function of the elevation and azimuth angles. For ambiguity calculation, it must be converted as a function of time and frequency using equations [15]–[17]. SW_i is the illuminated swath-width, α_f and α_n correspond to the core angles at far-range R_f and near-range R_n, respectively, γ_f and γ_n correspond to the look angles at $R_f$and R_n, respectively, β_i is the antenna elevation illumination beamwidth. Equation (18) assumes that the earth's radius is constant, which is an acceptable accurate approximation in LEO for swath-width less than 100 km.

AASR, RASR, and NESZ depend on the antenna gain, which is frequency dependent. The peak gain, 3 dB beamwidth and first sidelobe level significantly vary with the frequency. A typical way to estimate the system performance is to compute the ambiguities and NESZ for each frequency and take the average throughout the bandwidth, which involves significant computation. A more efficient way to estimate the system level performance would be to make use of the G^2 dependence on the antenna pattern gain and compute the frequency- independent bandwidth-integrated RMS peak gain and radiation patterns to compute the system performance. Swath-width requirement determines elevation antenna illumination beamwidth. The corresponding drop in the gain at the edges of the illumination beamwidth should be considered during NESZ computation. The RMS gain method is a reasonable approximation and significantly reduces the computation burden. Equations (13) and (14) compute the mean AASR and mean RASR over the Doppler processing bandwidth and receiving window corresponding to swath-width, respectively. For computing the maximum levels, spectral overlap between the signal and ambiguous return corresponding to the preceding and succeeding pulses must be considered, as shown in Fig. 11.

The MicroX-SAR system is designed for 1-m to 3-m ground range resolution with the off-nadir look angle varying from 15° to 45°. At a 30° off-nadir look angle, 1-m ground-range requires 300 MHz bandwidth from 9.5 to 9.8 GHz, while for 3-m ground-range resolution the bandwidth required is 100 MHz from 9.6 to 9.7 GHz. The bandwidth-integrated frequency-independent RMS radiation patterns are calculated for these two cases from the measurement data in steps of 50 MHz. The bandwidth-integrated RMS antenna efficiency for 3-m resolution and 1-m resolution are 53% and 47%, respectively, as shown in Fig. 6(g). Fig. 10(a) and (b) show the bandwidth-integrated RMS patterns along azimuth and elevation, respectively. The effect of higher sidelobes at 9.8 GHz in the elevation pattern is significantly suppressed in the RMS patterns; thus, undesired high sidelobes at one edge frequency does not significantly impact the overall system performance. These RMS patterns are used for estimating the system ambiguity levels.

Fig. 10(c) shows the variation of mean AASR with PRF for different combinations of ground-range resolution and azimuth processing bandwidth. The Nyquist sampling limit is $\frac{2V}{L_{\mathrm{az}}}$, i.e., 3104 Hz. Below this PRF, there is significant spectral overlap due to undersampling resulting in the high azimuth ambiguity level. For our mission, the maximum allowable mean AASR limit is –17.5 dB. This criterion is satisfied for PRFs greater than 3.5 kHz. Although the azimuth pattern has some undesired asymmetry due to unexpected phase variation among panels, it does not have any serious impact on the AASR or SAR imaging. Hence, aperture tapering is not necessary. Furthermore, aperture tapering would result in lowering the antenna gain, which would have a negative impact on the NESZ of the SAR image. Fig. 10(d) shows the variation of mean RASR with different combinations ground-range resolution and swath-width at an off-nadir look angle of 30°. The desired mean RASR limit less than –17.5 dB limit is achieved for PRF less than 5 kHz.

PRF selection is another important aspect for SAR mission design. There are several PRF constraints for a mono-static SAR which makes PRF selection quite challenging and critical, as explained in [18]. Furthermore, it is seen that azimuth ambiguities decrease with an increase in PRF whereas range ambiguities increase with an increase in PRF. As the swath-width increases, the receiving window also increases. Also, for a fixed swath-width as the off-nadir look angle increases or if the satellite altitude increases, the receiving window increases. As a result, it becomes quite difficult to use high PRF. NESZ degrades if: satellite altitude increases; the off-nadir look angle becomes higher or chirp bandwidth is increased, i.e., finer ground-range resolution is desired. Since the peak power is fixed, to compensate this, higher transmission duty cycle needs to be used and this further makes it difficult to use high PRF. So, acceptable AASR limit becomes critical for PRF selection. Unlike AASR, RASR is highly sensitive to the off-nadir look angle and relatively sensitive to change in the satellite altitude.

Fig. 10(e) shows the sample PRF selection computation at the 30° off-nadir look angle for different combinations of ground-range resolution and swath-widths using the mission parameters in Table I. The maximum acceptable limits of peak AASR and peak RASR are considered in PRF selection. Fig. 11(a)–(f) show the overlap of the spectral overlap of the signal with the ambiguous return in range-time domain, and Fig. 11(g) and (h) show the same in the azimuth Doppler frequency domain. As seen, the maximum ambiguity signal overlaps occur at the edges of the receiving window and Doppler bandwidth. A total of 4457 Hz is a suitable PRF because: it is low enough to permit 28 km swath-width acquisition; and the maximum ambiguity signal power levels are below –20 dB in the range time receiving window and azimuth frequency processing bandwidth. From Fig. 11(g) and (h), it can be concluded that the impact of asymmetric azimuth main beam is within permissible limits since

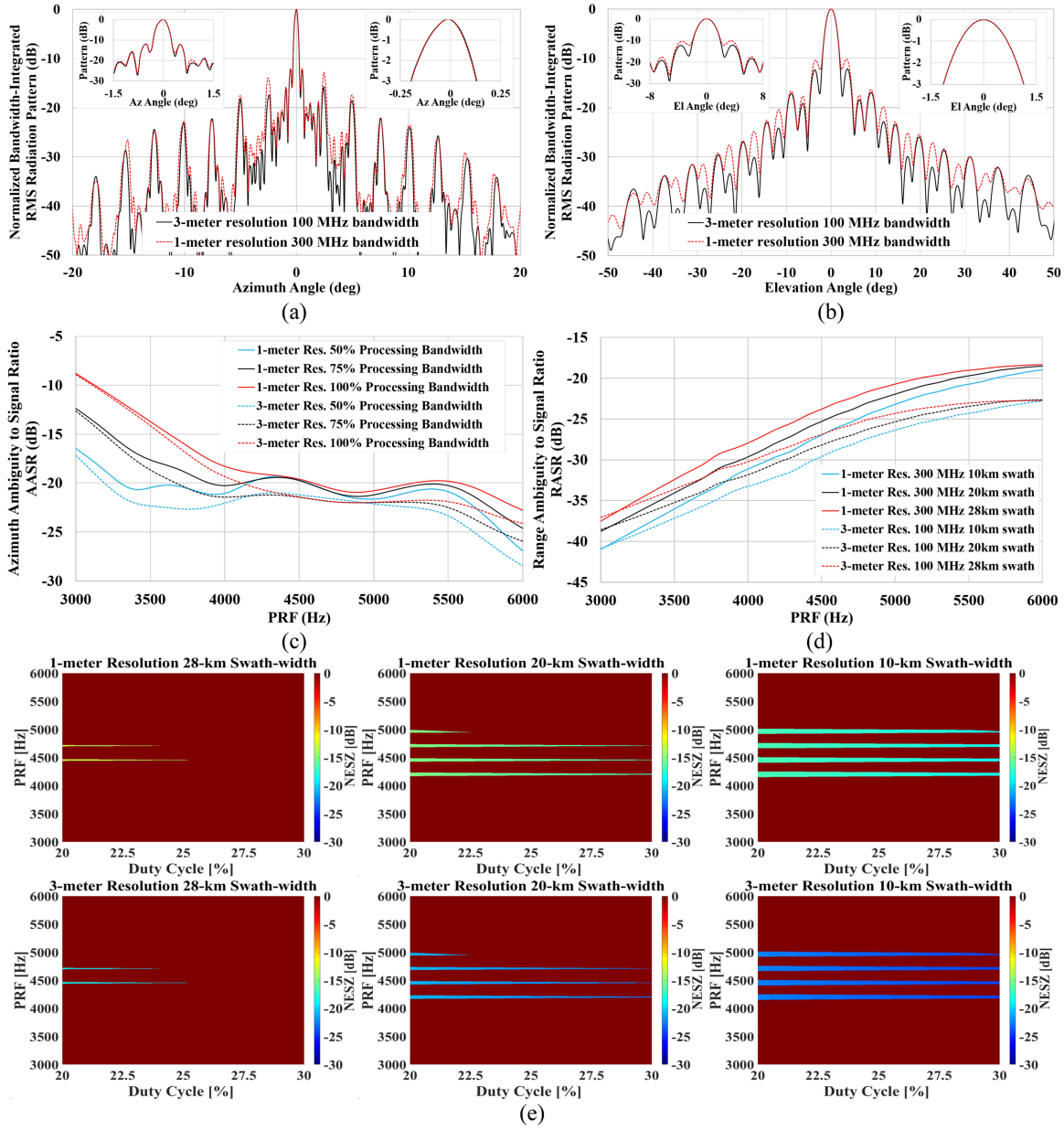

Fig. 10. (a) Bandwidth-integrated RMS azimuth pattern. (b) Bandwidth-integrated RMS elevation pattern. (c) Mean AASR versus PRF for different ground-range resolution and processing bandwidths at 510 km altitude. (d) Mean RASR versus PRF for different ground-range resolution and swath-widths at 510 km altitude 30° off-nadir look angle. (e) PRF selection and mean NESZ level for different ground-range resolutions and swath-widths at 510 km altitude 30° off-nadir look angle.

both the maximum peak AASR and maximum peak RASR are below –15 dB limit as desired. Table III summarizes the system performance for potential modes of operation. Since the NESZ and ambiguity levels vary significantly over the range swath and azimuth processing bandwidth, both the mean values and maximum peak (worst case) values are provided. The maximum capability of the present system is 1-m resolution ground-range resolution with 28 km swath-width at an altitude of 510 km with an operating PRF 4.457 kHz with 25% duty cycle at the 30° off-nadir look angle with mean NESZ, AASR, and RASR levels of –14, –21, and –24 dB, respectively, and maximum NESZ, AASR, and RASR levels of –13, –15, and –16 dB, respectively.

Fig. 10(e) shows that 28 km swath is a limiting factor for PRF selection at 25% duty cycle due to interference between RX signal and TX signal. Thus, the only feasible solution to achieve large swath is to increase the transmission peak power adequately to improve NESZ while lowering the duty cycle simultaneously to ensure PRFs greater than 3.5 kHz are permissible. This is currently being investigated to make the system capable of 40 km swath width for future missions. For wide swath acquisition at off-nadir angles greater than 35°, the range ambiguous overlap in time-domain occurs with the main lobe of the antenna pattern at the swath edge. Thus, range ambiguity suppression using up-down chirp as proposed in [18] might be necessary.

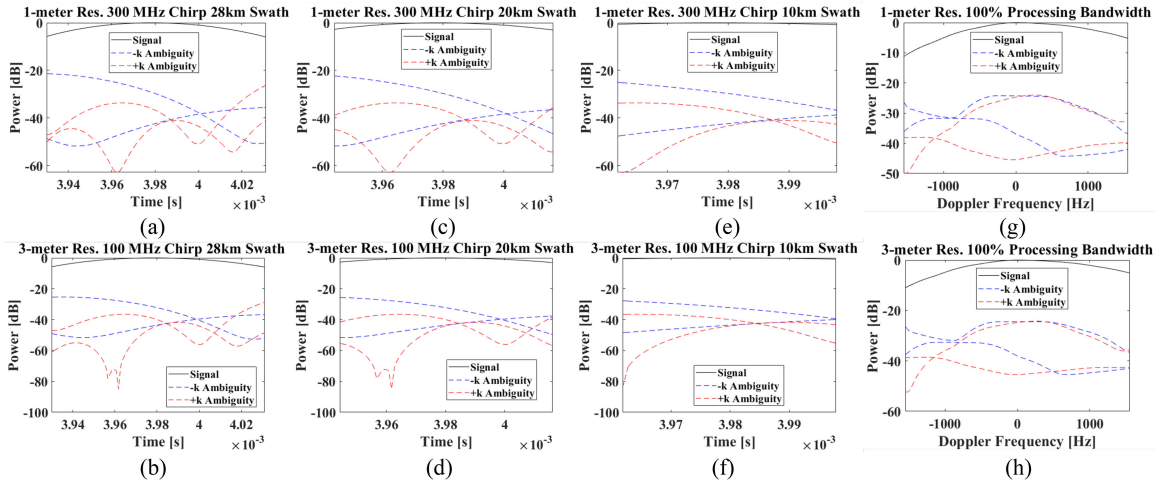

Fig. 11. (a)–(f) Spectral overlap of signal and ambiguous return in range time domain receiving window. (g)–(h) Spectral overlap of signal and ambiguous return in azimuth frequency domain Doppler bandwidth. The first two succeeding and preceding pulses are considered ($k = 1, 2$) at PRF = 4457 Hz at 510 km altitude 30° off-nadir angle for different resolutions and swath widths. Processed Doppler bandwidth is 3104 Hz, Azimuth resolution is 2.45 m, strip-map mode.

TABLE III
MICROX-SAR SYSTEM PERFORMANCE

SW (km)	Gr. Res. (m)	NESZ Center (dB)	NESZ Max (dB)	AASR Max (dB)	AASR Mean (dB)	RASR Max (dB)	RASR Mean (dB)	RW (μs)
28	1	-18.8	-13	-15.3	-21.4	-16	-24	101
28	3	-24.6	-18.8	-16	-22	-20	-27	101
20	1	-18.8	-15.8	-15.3	-21.4	-19.6	-26	72
20	3	-24.6	-21.6	-16	-22	-22.9	-28.8	72
10	1	-18.8	-18.1	-15.3	-21.4	-24	-27.6	36
10	3	-24.6	-23.9	-16	-22	-26.7	-30.2	36

(510 km altitude, 30° off-nadir look angle, and 25% TX duty cycle at 4457 Hz PRF, RW is receiving window, processed Doppler bandwidth is 3104 Hz, Azimuth resolution is 2.45 m, strip-map mode).

IV. CONCLUSION

This article shows the development and performance evaluation of prototype flight model antenna system of MicroX-SAR Mission. Seven-panel antenna array performance was accurately estimated by means of synthesis from the single-panel measurement results and cascaded scattering matrix. The synthesis methodology was verified by confirming with measurement results. SAR image performance indices like NESZ, ambiguities were estimated from the bandwidth-integrated radiation patterns. PRF selection was performed at an altitude of 510 km and 30° off-nadir look angle. Although the antenna pattern has azimuth asymmetry with relatively higher than expected first SLL in elevation and azimuth, especially at the edge frequency due to phase imbalance caused by fabrication imperfections, the effect is significantly mitigated in the bandwidth-integrated frequency-independent RMS antenna patterns used for system performance evaluation. Furthermore, careful PRF selection ensured that azimuth ambiguity and range ambiguity levels are within acceptable limits. Following several system tradeoffs, the maximum capability of the present system was determined to be 1-m ground-range resolution with 28 km swath-width. On-board SAR instruments were verified by a SAR imaging test with a point source simulator. The first demonstration flight of the MicroX-SAR system is scheduled to be in 2020 as collaboration with Synspective Inc. [5].

ACKNOWLEDGMENT

The author would like to thank H. Sakamoto of NSI-MI Japan for his dedicated assistance during conducting the near-field measurements and solving key issues concerning the NSI-MI plane-polar near-field measurement software.

REFERENCES

[1] B. Grafmuller, A. Herschlein, and C. Fischer, "The TerraSAR-X antenna system," in *Proc. IEEE Int. Radar Conf.*, May 2005, pp. 222–225.
[2] H. M. Braun and P. E. Knobloch, "SAR on small satellites- shown on the SAR-Lupe example," in *Proc. Int. Radar Symp.*, Cologne, Germany, Sep. 2007, pp. 5–7.
[3] U. Naftaly and R. Levy-Nathansohn, "Overview of the TECSAR satellite hard-ware and mosaic mode," *IEEE Geosci. Remote Sens. Lett.*, vol. 5, no. 3, pp. 423–426, Jul. 2008.
[4] P. Davies *et al.*, "NovaSAR-S bringing radar capability to the disaster monitoring constellation," in *Proc. 4S Symp.*, Jun. 2012.
[5] [Online]. Available: https://synspective.com/, Accessed on: Jul. 8, 2020.
[6] G. Farquharson, W. Woods, C. Stringham, N. Sankarambadi, and L. Riggi, "The Capella synthetic aperture radar constellation," in *Proc. IEEE Int. Geosci. Remote Sens. Symp.*, Valencia, Spain, 2018, pp. 1873–1876.
[7] O. Antropov, J. Praks, M. Kauppinen, P. Laurila, V. Ignatenko, and R. Modrzewski, "Assessment of operational microsatellite based SAR for earth observation applications," in *Proc. 2nd URSI Atlantic Radio Sci. Meeting*, Meloneras, Spain, 2018.
[8] [Online]. Available: https://space.skyrocket.de/doc_sdat/qps-sar-1.htm, Accessed on: Jul. 8, 2020.
[9] H. Saito *et al.*, "Development of compact SAR systems for small satellite," in *Proc. IEEE Int. Geosci. Remote Sens. Symp.*, Yokohama, Japan, 2019, pp. 8440–8443.
[10] P. R. Akbar, H. Saito, M. Zhang, J. Hirokawa, and M. Ando, "Parallel-plate slot array antenna for deployable SAR antenna onboard small satellite," *IEEE Trans. Antennas Propag.*, vol. 64, no. 5, pp. 1661–1671, May 2016.
[11] B. Pyne, P. Akbar, H. Saito, M. Zhang, J. Hirokawa, and M. Ando, "Design of a center-feed waveguide feeder for wideband rectangular parallel-plate slot-array antenna on-board space-borne X-band SAR system," in *Proc. 46th Eur. Microw. Conf.*, London, U.K., 2016, pp. 1533–1536.
[12] B. Pyne, V. Ravindra, P. A. Riziki, H. Saito, and J. Hirokawa, "Performance analysis of edge-feed rectangular parallel plate slot-array antenna panel for compact space-borne x-band SAR system," in *Proc. Int. Conf. Electromagn. Adv. Appl.*, Verona, Italy, 2017, pp. 407–410.
[13] P. R. Akbar, B. Pyne, H. Saito, J. Hirokawa, and D. Kim, "Present state of antenna design for X-band SAR sensor onboard 100 Kg class satellite," in *Proc. 11th Eur. Conf. Antennas Propag.*, Paris, France, 2017, pp. 2640–2641.

[14] B. Pyne, P. R. Akbar, V. Ravindra, H. Saito, J. Hirokawa, and T. Fukami, "Slot-array antenna feeder network for space-borne X-band synthetic aperture radar," *IEEE Trans. Antennas Propag.*, vol. 66, no. 7, pp. 3463–3474, Jul. 2018.

[15] B. Pyne, R. Naruse, H. Saito, J. Hirokawa, V. Ravindra, and P. R. Akbar, "Robust contactless noncircular choke flange for wideband waveguide applications," *IEEE Trans. Microw. Theory Techn.*, vol. 67, no. 3, pp. 861–867, Mar. 2019.

[16] V. Ravindra, H. Saito, J. Hrokawai, M. Zhang, and Atsushi Tomiki, "A TM010 cavity power-combiner with microstrip line inputs," *IEICE Trans. Electron., 2017ECP5025*, vol. E100-C, no. 12, pp. 1087–1096, 2017.

[17] J. C. Curlander and R. N. McDonough, *Synthetic Aperture Radar Systems and Signal Processing*. NJ, USA: Wiley, 1991, pp. 294–306.

[18] B. Pyne, V. Ravindra, and H. Saito, "An improved pulse repetition frequency selection scheme for synthetic aperture radar," in *Proc. 12th Eur. Radar Conf.*, Paris, France, Sep. 2015, pp. 257–260.

[19] H. Saito, T Fukami, H. Watanabe, T. Mizuno, A. Tomiki, and N. Iwakiri, "World fastest communication from a 50 kg class satellite—Micro satellite Hodoyoshi-4 succeeds in 348 Mbit per seconds," *IEICE Commun. Soc. Global Newslett.*, vol. 39, no. 2, pp. 25–30, 2015.

[20] H. Saito, T Fukami, H. Watanabe, T. Mizuno, A. Tomiki, and N. Iwakiri, "High bit-rate communication in X band for small earth observation satellites—Result of 505 Mbps demonstration and plan for 2 Gbps link," in *Proc. AIAA/Utah State Univ. Small Satellite Conf.*, Utah, Logan, USA, Aug. 2016.

[21] T. Kaneko *et al.*, "2Gbps downlink system of 100kg class satellite for compact synthetic aperture radar mission," in *Proc. Small Satellites Syst. Serv.– 4S Symp.*, Sorrento, Italy, May 28–Jun. 1, 2018, Paper 48.

[22] T. Kaneko *et al.*, "2Gbps downlink system of 100kg class satellite for compact synthetic aperture radar mission," in *Proc. Small Satellites Syst. Serv.– 4S Symp.*, Sorrento, Italy, May 28–Jun. 1, 2018, Paper 48.

Budhaditya Pyne (Member, IEEE) was born in Kolkata, India, in 1991. He received the B.E. degree in electrical engineering from Jadavpur University, Kolkata, India, in December 2013, and the M.E. and Ph.D. degrees in electrical engineering and information systems from the University of Tokyo, Tokyo, Japan, in 2015 and 2018, respectively.

From December 2017 to March 2018, he was a Guest Scientist with the Department of Radar Concepts for SAR Missions, DLR Microwaves and Radar Institute, Oberpfaffenhofen, Germany. From December 2018 to March 2019, he was a Project Research Associate with the Department of Spacecraft Engineering, Institute of Space and Astronautical Science (ISAS), Japan Aerospace Exploration Agency (JAXA). Since April 2019, he has been working as a RF Engineer with the Department of Satellite Systems Development, Synspective Inc., Tokyo, Japan. His research focuses on the development of the SAR RF antenna system for small satellites and SAR signal processing.

Dr. Pyne is a member of the IEEE Antennas and Propagation Society, Microwave Theory and Techniques Society, Geoscience and Remote Sensing Society, Aerospace and Electronic Systems Society, and European Microwave Association.

Hirobumi Saito (Member, IEEE) received the B.S., M.S., and Ph.D. degrees in electrical engineering from the University of Tokyo, Tokyo, Japan, in 1976, 1978, and 1981, respectively.

He is currently a Professor with the Spacecraft Engineering Division, Institute of Space and Astronautical Sciences (ISAS), Japan Aerospace Exploration Agency (JAXA), Tokyo, Japan. He was a Visiting Research Scientist with MIT from 1986 through 1988, and a Visiting Research Scientist with the Jet Propulsion Laboratory (JPL), California Institute of Technology (CALTECH), in 1991. He is currently engaged in research on high-bit rate downlink communications and SAR system onboard a small satellite. He has authored and coauthored more than 50 scientific papers and two books.

Dr. Saito was the recipient of the Technology prize of the Japan Society for Aeronautical and Space Sciences, in 2010, and the Minister prize of Education, Science and Technology, Japan, in 2012. He is a member of International Academy of Astronautics and IEICE.

Prilando Riziki Akbar (Member, IEEE) was born in Jakarta, Indonesia, in 1979. He received the B.E. degree in electrical engineering from STT Telkom, Bandung, Indonesia, in 2001, and the M.E. and Ph.D. degrees in information science from Chiba University, Chiba, Japan, in 2009 and 2012, respectively.

From 2001 to 2009, he was with a renowned telecommunication industry in Indonesia. In 2012, he joined the Center for Environmental Remote Sensing, Chiba University, as a Research Fellow. In 2013, he became a Project Research Associate with the Department of Spacecraft Engineering, Institute of Space and Astronautical Science, Japan Aerospace Exploration Agency, Sagamihara Campus, Japan. From April 2018 to March 2019, he was a Project Senior Assistant Professor with the Graduate School of System Design and Management, Keio University, Japan. Since April 2020, he has been a RF Engineer with the Department of Satellite Systems Development, Synspective Inc., Tokyo, Japan. His current research interests include the development of antenna for synthetic aperture radar for small satellites.

Jiro Hirokawa (Fellow, IEEE) was born in Tokyo, Japan, on May 8, 1965. He received the B.S., M.S., and Ph.D. degrees in electrical and electronic engineering from the Tokyo Institute of Technology, Tokyo, Japan, in 1988, 1990, and 1994, respectively.

From 1994 to 1995, he was with the Antenna Group, Chalmers University of Technology, Gothenburg, Sweden, as a Postdoctoral Fellow. He is currently a Professor with the Tokyo Institute of Technology. His research area has been in slotted waveguide array antennas and millimeter-wave antennas.

Dr. Hirokawa was the recipient of an IEEE AP-S Tokyo Chapter Young Engineer Award, in 1991, a Young Engineer Award from IEICE, in 1996, Tokyo Tech Award for Challenging Research, in 2003, a Young Scientists' Prize from the Minister of Education, Cultures, Sports, Science and Technology, in Japan in 2005, a Best Paper Award, in 2007, a Best Letter Award, in 2009 from IEICE Communications Society and Asia Pacific Microwave Conference Prize, in 2011, 2012, and 2013, respectively. He is a Fellow of IEICE.

Takashi Tomura (Member, IEEE) was born in Sendai, Japan. He received the B.S., M.S., and D.E. degrees in electrical and electronic engineering from the Tokyo Institute of Technology, Tokyo, Japan, in 2008, 2011, and 2014, respectively.

From 2014 to 2017, he was with Mitsubishi Electric Corporation, Tokyo, Japan, and was involved in the research and development of aperture antennas for satellite communications and radar systems. He is currently a Specially Appointed Assistant Professor with the Tokyo Institute of Technology, Tokyo, Japan. His current research interests include electromagnetic analysis, aperture antennas, and planar waveguide slot array antennas.

Dr. Tomura is a member of IEICE. He was a Research Fellow with the Japan Society for the Promotion of Science, in 2013. He was the recipient of the Best Student Award from Ericsson Japan, in 2012 and the IEEE AP-S Tokyo Chapter Young Engineer Award, in 2015.

Koji Tanaka (Member, IEEE) was born in Japan, in 1963. He received the Ph.D. degree in electrical engineering from Niigata University, Niigata, Japan, in 1999.

Since 2003, he has been an Associate Professor with the Department of Space Information and Energy, Institute of Space and Astronautical Science (ISAS), Japan Aerospace Exploration Agency (JAXA), Kanagawa, Japan. His research interests include space power systems and the interactions between high-power systems and space environments.